Ionospheric response to wave-accelerated electrons at the poleward auroral boundary

J. Semeter,[1] C. J. Heinselman,[2] G. G. Sivjee,[3] H. U. Frey,[4] and J. W. Bonnell[4]

Received 11 May 2005; revised 8 July 2005; accepted 1 August 2005; published 26 November 2005.

[1] The local ionospheric response to an auroral intensification at the poleward auroral boundary has been investigated using the incoherent scatter radar (ISR) and optical instrumentation at Sondrestrom, Greenland, in conjunction with space-borne measurements by the IMAGE and FAST satellites. ISR elevation scans through the illuminated region revealed filamentary columns of enhanced plasma density, ~5 km in latitude by ~200 km in altitude. Column densities were typically $5 \times 10^{11}/m^3$ above background and often constant over a broad range of altitudes. The brightness of the O^+ 732–733 nm multiplet, monitored simultaneously by a near-infrared spectrometer, exceeded 1.2 kR during one 4-min period (a factor of ~4 brighter than previously reported auroral measurements). A time-dependent model was developed to relate O^+ emission intensities to O^+ column densities for a given illumination time. The results suggested that the electron source was composed of kilometer-scale flux tubes locked in the $E \times B$ flow for several minutes whose average energy varied temporally between <100 eV and >1 keV over their illumination lifetime. Conjugate electrons measured by the FAST satellite at 1700 km showed evidence for energization by inertial Alfvén waves. Ionization rates computed from these spectra were sufficient to account for the observed filamentary ionospheric structure. The implications of such ionization patterns for electrodynamic coupling with the magnetosphere are discussed.

Citation: Semeter, J., C. Heinselman, G. G. Sivjee, H. U. Frey, and J. W. Bonnell (2005), Ionospheric response to wave-accelerated electrons at the poleward auroral boundary, *J. Geophys. Res.*, *110*, A11310, doi:10.1029/2005JA011226.

1. Introduction

[2] During periods of prolonged magnetospheric activity, the nightside auroral oval often develops a double configuration, with a latitudinally narrow band demarcating the open-closed field-line boundary, and a broader diffuse band of emission to the south [*Yamamoto et al.*, 1993; *Elphinstone et al.*, 1995]. The poleward band may be composed of periodic intensifications reminiscent of pearls on a string or north-south ''streamers'' that sometimes span the entire width of the oval [*Henderson et al.*, 1998]. Temporal variability in these large-scale features appears to be correlated with ULF pulsations [*Lyons et al.*, 2002]. *Lyons et al.* [2000] have applied the term ''poleward boundary intensification'' (PBI) to this class of auroral morphology.

[3] In contrast to ''inverted-V'' electron spectra associated with arcs in the main auroral oval, electron spectra measured near the poleward auroral boundary show evidence for acceleration by Alfvén waves [*Chaston et al.*, 2002]. In the satellite reference frame, wave accelerated electrons appear as time-dispersive, field-aligned bursts (FABs) spanning a broad range of energies [*Arnoldy et al.*, 1999]. The spatial and spectral characteristics of optical auroras near the polar cap boundary appear to be consistent with such a particle source [e.g., *Zesta et al.*, 2002; *Semeter*, 2003]. Hence the term ''Alfvénic aurora'' has also been applied to these auroral forms.

[4] Previous investigations into auroral poleward boundary intensifications have focused almost exclusively on the underlying magnetospheric dynamics. This article focuses, instead, on the ionospheric response to these auroras. Using a combination of ground-based and space-borne diagnostics, we have conducted a quantitative analysis of the causal chain connecting particle energy spectra to observed ionization patterns. The investigation grew from incoherent scatter radar observations of latitudinally narrow plasma enhancements extending from the lower E region through the F region. These filamentary structures support some of the strongest horizontal gradients observed anywhere in the ionosphere. The presence of these gradients in regions of impinging Alfvén waves adds a degree of complexity to the electrodynamic coupling between the magnetosphere and ionosphere.

[5] A secondary objective of this article is to present a simple framework for fusing space-borne and ground-based measurements of the magnetosphere-ionosphere system

[1]Department of Electrical and Computer Engineering and Center for Space Physics, Boston University, Boston, Massachusetts, USA.
[2]SRI International, Menlo Park, California, USA.
[3]Embry-Riddle Aeronautical University, Daytona Beach, Florida, USA.
[4]Space Sciences Laboratory, University of California, Berkeley, Berkeley, California, USA.

0148-0227/05/2005JA011226$09.00

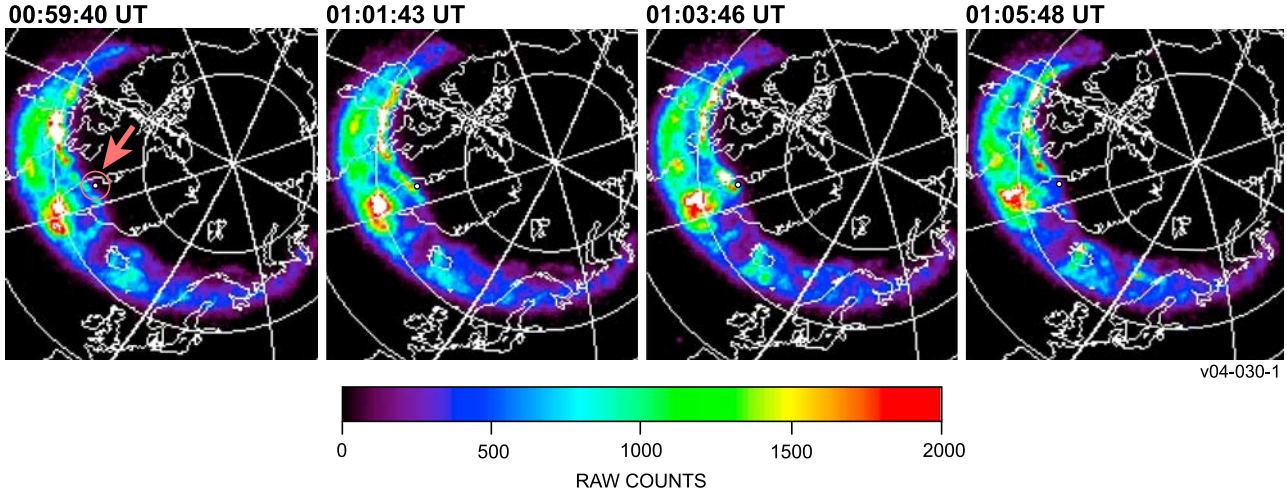

Figure 1. The far ultraviolet auroral oval at 2-min intervals recorded by the IMAGE satellite, showing the evolution of auroral intensification along the polar cap boundary. Sondrestrom is indicated by a white dot in each image, and the 150 km field-of-view of the all-sky imager is indicated by the red circle in the first panel.

through a coupled model of electron penetration, ionospheric continuity, and photochemical equilibrium. In the present context, this framework is used to evaluate the self-consistency of in situ electron, ground-based optical, and ground-based radar measurements.

2. Experiment Description

[6] This work is based on an experiment conducted on 19–20 November 2001 at the Sondrestrom, Greenland, incoherent scatter radar (ISR) facility. Sondrestrom lies near the nominal open-closed field-line boundary at all local times. In addition to the 1.3 GHz ISR, the facility hosts a comprehensive set of optical instruments, making it ideal for coordinated radar and optical studies of the auroral ionosphere. For this experiment, the ISR was scanned continuously along the magnetic meridian (azimuth 141°) between 29° and 83° equatorward elevation. Each scan lasted 2 min. The scan duration was chosen to balance the competing requirements of SNR and temporal resolution. The radar was operated with a 50 μs pulse modulated with a 5-baud Barker code. Matched filtering provided independent samples of backscattered power at 1.5 km range resolution out to a maximum range of ~350 km. The data were converted to electron densities by applying appropriate scaling and range correction terms.

[7] The principal uncertainty in using backscattered power as an estimate of plasma density lies in the lack of knowledge of the electron-to-ion temperature ratio. In our analysis we assumed $T_e/T_i = 1$, which is generally valid below 150 km. For altitudes >150 km we expect $T_e > T_i$, which would lead to an underestimation of our plasma densities. Because we are primarily interested in plasma enhancements, of greater concern are cases where our analysis overestimates density, i.e., where $T_i > T_e$. Such conditions may occur in regions of extremely large electric fields. However, even under a worst-case scenario of $T_i = 3T_e$, the radar cross section (and hence density) would be overestimated by only ~30% [*Evans* 1969, Figure 4]. This level of error does not affect the conclusions of this work.

[8] In addition to the ISR, two collocated optical instruments were used. First, the Sondrestrom all-sky imager (ASI) recorded images at 1 frame/s through a red glass filter with a short wavelength cutoff of 640 nm. This filter suppressed the bright metastable transitions at 630 nm and 557.7 nm, passing primarily the prompt emission bands of the N_2 first positive group (1PG). Such a filtering strategy allowed us to directly relate auroral morphology with electron precipitation patterns. The ASI also provided a quantitative estimate of the residency time of auroral forms within the radar scan volume.

[9] Second, a near-infrared spectrometer was used to monitor the intensity of atomic oxygen emissions in the magnetic zenith [*Sivjee and Shen*, 1997]. Of particular interest was the O^+ 732–733 nm multiplet, used to estimate the line-of-sight integrated production rate of O^+ ions.

[10] Ground-based measurement were augmented by two space-borne diagnostics. The Wide-Band Imaging Camera (WIC) on the IMAGE satellite provided the global-scale auroral morphology. In situ electron measurements were provided by the Electron ESA Spectrometer (EES) instrument on the FAST satellite.

3. Data Overview

[11] Figure 1 shows samples of the far ultraviolet auroral oval during a 10 min interval on 19 November 2001. Sondrestrom is indicated by a white dot in each image, and the 150 km field-of-view of the Sondrestrom ASI is given by the red circle in the first image. Time labels correspond to the center integration time of each 10 s exposure. The WIC is sensitive to the N_2 LBH band, excited most efficiently by primary electrons in the keV energy range. The sequence documents intensifications along the poleward auroral boundary observed during the recovery phase of a substorm. The bright spot near the zenith of Sondrestrom at 0103:46 UT is the focus of this study.

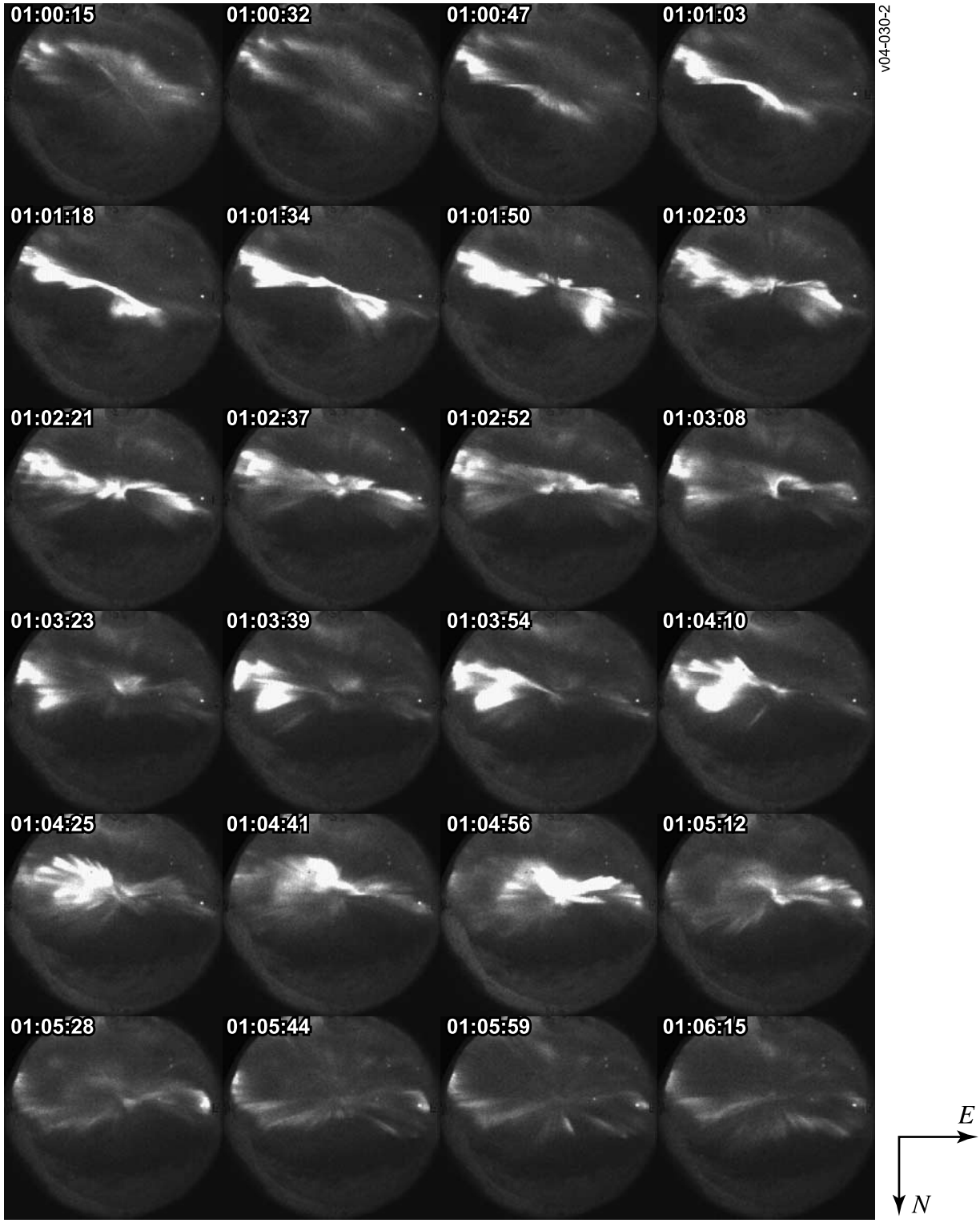

Figure 2. Sample all-sky images at 15 s intervals during a 6 min period encompassing the interval in Figure 1. Images were recorded through a red glass filter with short wavelength cutoff at 640 nm. (Note that images are displayed in their native horizon-based coordinate system; hence east and west are reversed compared to the compass.)

[12] Figure 2 shows how this PBI event appears from the ground-based perspective. The figure presents 15 s samples from the ASI encompassing the period of Figure 1. The initial intensification is documented in the first four images, after which the PBI evolves into a collection of rayed auroral forms comprising an east-west band near the zenith (center of the image). Note that despite variability in the morphology and intensity of the substructures, the aggre-

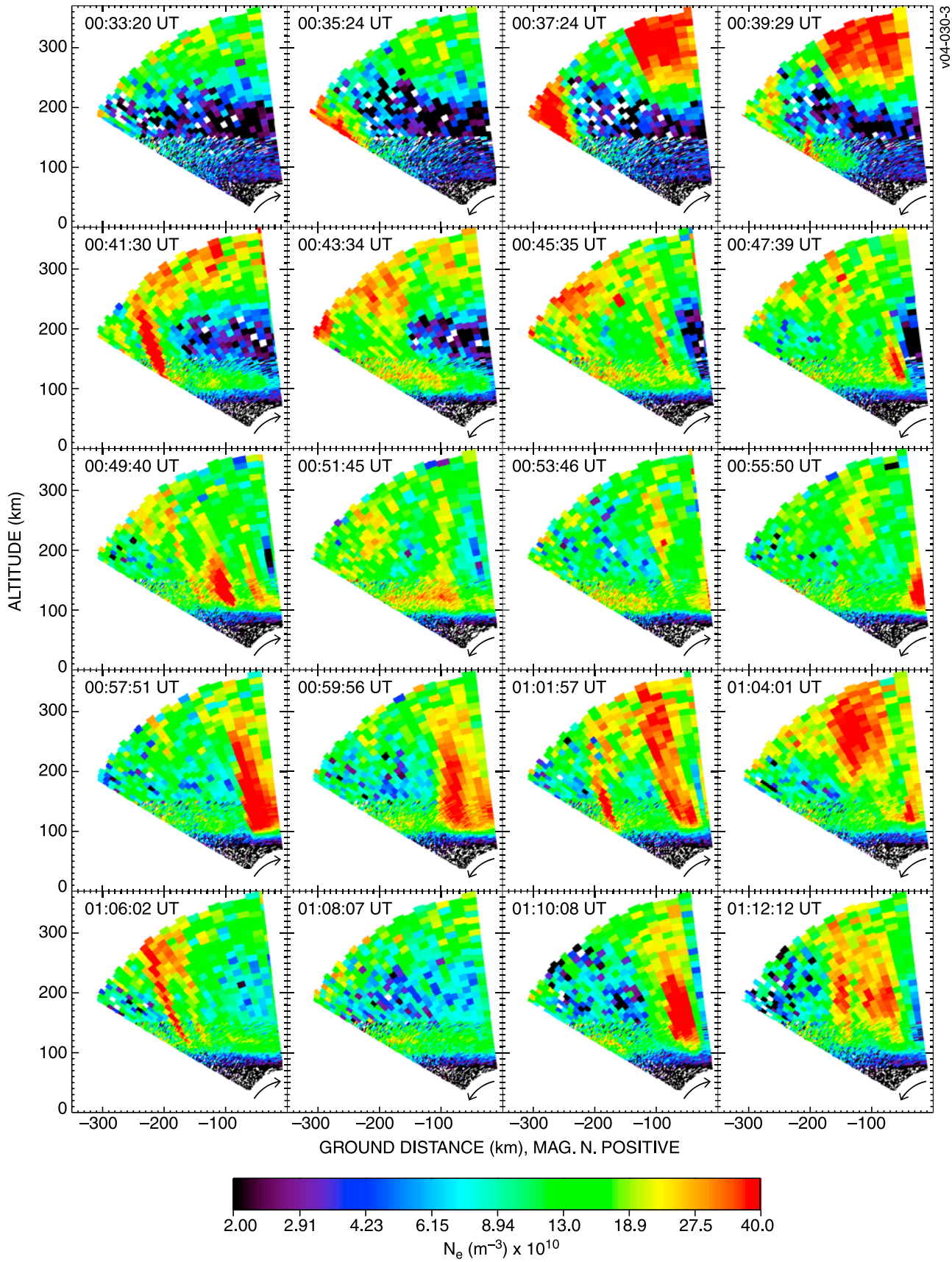

Figure 3. Electron density derived from elevation scans by the Sondrestrom ISR. Each scan lasted ~2 min, with scan direction as indicated.

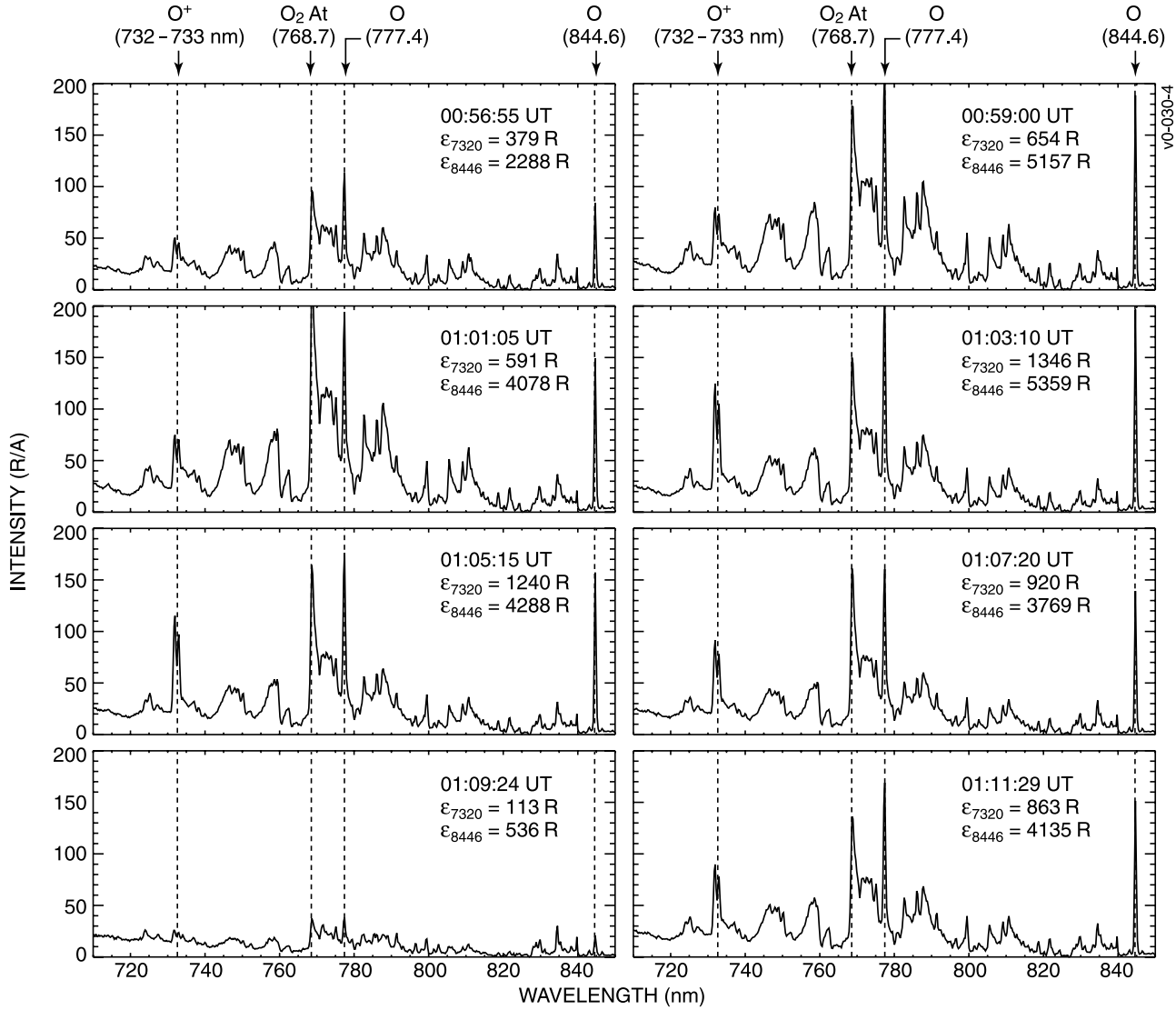

Figure 4. Near infrared spectra (2-min exposures) recorded during the period of Figure 2. The integrated intensity of the O^+ 732–733 nm multiplet and the OI 844.6 nm emission are as indicated. The OI 844.6 nm intensity has been reduced by a factor of 10 in these plots for display purposes.

gate location of the emission band remains near the zenith throughout this 6-min sequence. This observation becomes important in explaining the observed response of the ionosphere.

[13] Figure 3 summarizes ISR measurements of the ionospheric plasma density associated with the auroral display in Figure 2. The data were processed at 5 s time integration and two different range integrations: 1.5 km below 150 km and 10 km above 150 km. The inset arrow indicates the scan direction in each image.

[14] The first panel constitutes a preevent scan: there is no detectable auroral *E* region, and the *F* region consists of a uniform quiescent layer with a peak density of $\sim 10^{11}$ m^{-3}. The next three panels document what, in this reference frame, appears to be the poleward approach of the open-closed field-line boundary, as evidenced by the sharp ledge in *E* region density. In subsequent panels, field-aligned density structures of varying altitudes, widths, and intensities are seen embedded within this uniform auroral *E* layer. The simultaneous presence of these two types of auroral ionization indicates the simultaneous presence of soft and hard particle fluxes with very different spatial structure. That the softer precipitation is more structured than the harder precipitation is unexpected; in the main auroral oval it is the harder, more energetic electrons that exhibit the higher degree of structure.

[15] The embedded ionization columns in Figure 3 are the primary focus of this work. In many cases, these columns can be seen to extend from 100 km to >300 km (see, e.g., 0049:40, 0101:57, 0106:02). Of course, one must be cautious about interpreting Figure 3 as two-dimensional "snapshots." The general motion of auroral structures in this interval was southward, consistent with the general description of PBI aurora given by *Zesta et al.* [2002]. Equatorward motion will distort field-aligned structure in a manner that depends on the antenna scan direction: for downward (upward) scans, the field-aligned columns will appear tipped to the north (south) compared to the magnetic

dip angle (~9.6° at 300 km) and broadened (narrowed) horizontally. This effect is readily seen by comparing downward and upward scans in Figure 3 (e.g., panels at 0049:40 UT and 0051:45 UT).

[16] Above ~250 km, structure in the high-latitude plasma is usually attributed to horizontal transport effects. Specifically, the transport of *F* region plasma patches out of the polar cap under the action of reconnection, and their subsequent deformation in the sunward convection region, leads to latitudinally confined, longitudinally extended ionization patterns consistent with present observations above 250 km [*Robinson et al.*, 1985; *Crowley et al.*, 2000; *Semeter et al.*, 2003]. That the columns in Figure 3 are contiguous between the production-dominated *E* region and the transport-dominated *F* region suggests an auroral source for the entire altitude range. To produce a uniform density enhancement over such a broad altitude range places strict requirements on the energy, number flux, and temporal stability of the causative particle source. Before addressing this, it is prudent to first verify our interpretation of the ISR results using other diagnostics.

[17] Figure 4 presents spectra recorded in the magnetic zenith by the near-infrared spectrometer for this period. The dominant line spectra are produced by atomic oxygen. Of particular interest is the O^+ 732–733 nm emission, excited by impact ionization of atomic oxygen. This quadruplet emission appears as a single line at the resolution of this instrument. The oxygen line emissions are superposed on the broad bands of the N_2 first positive group (1PG) system. The O^+ 732–733 nm emission originates in the *F* region and is associated with auroral primaries in the <100 eV range; the N_2 1PG emission originates in the *E* region and is associated auroral primaries in the >1 keV range [*Semeter*, 2003].

[18] In the first three panels of Figure 4, there is a general increase in intensity of all emission features present, indicating the presence of an electron flux with a broad energy distribution. Comparing the third and fourth panels, the N_2 1PG decreases while the oxygen emissions continue to increase, indicating a change in the incident energy spectrum. In the 0103:10 UT and 0105:15 UT spectra, the O^+ 732–733 nm brightness exceeded 1.2 kR. This is a factor of ~4 brighter than any previous reported measurements we are aware of. Indeed, owing to the 2 min integration period the peak brightness was likely even greater. We thus have evidence for an intense ionizing flux impinging the oxygen-dominated *F* region for a period of several minutes. Next, we investigated whether this O^+ source was sufficient to account for the columns in Figure 3.

4. Combined Analysis of Radar and Optical Measurements

[19] Figures 1–4 give four distinct perspectives of the same event. Comparing these figures, we observe the following. The largest O^+ 732–733 nm intensity in Figure 4 was coincident with a global scale intensification of the poleward auroral boundary (Figure 1, ~0103:46 UT). Locally, this intensification was manifested as a band of rayed auroral forms (Figure 2, 0101:03 to 0104:56 UT). During this period the ISR measured ionization columns with the largest density (Figure 3, 0101:57 scan). In this section, we describe our approach to evaluating the self-consistency of these independent measures of ion production, ion density, and auroral morphology.

4.1. Extracting Columnar Plasma Density

[20] We focused our analysis on the 0101:57–0103:57 UT scan in Figure 3. This period was characterized by both the largest *F* region density enhancement and the largest O^+ 732–733 nm intensity. Because of the exceptional signal to noise ratio for this scan, we have reprocessed the ISR data at 1 s resolution, shown in Figure 5a. We now see that the broad column of ionization in Figure 3 is, in fact, composed of at least two narrow adjacent columns, each extending through the maximum observable range. This result emphasizes that the ISR, in general, undersamples the horizontal variability in auroral ionization patterns.

[21] In Figure 5b, the red line gives the background-subtracted electron density profile through the column demarcated by the red arrows in Figure 5a. Owing to possible distortions introduced by motion of the flux tube during the scan, densities were not extracted strictly along a line of constant dip angle, but rather they were hand picked to best trace the columnar density enhancement.

[22] The black curve in Figure 5b plots the portion of total plasma density in this column that is O^+; the blue curve plots the molecular ion density (essentially equal to $[NO^+] + [O_2^+]$). This partitioning was computed using the empirical model of [*Kelly and Wickwar*, 1981], reproduced in Figure 6. The curve reflects the average composition derived from many measurements by the Chatanika radar under various auroral conditions. The actual partitioning is expected to scale somewhat with exospheric temperature and with the intensity and time-history of particle precipitation and joule heating. Under the large electric field conditions expected here, O^+ can rapidly become NO^+ due to a ~16-fold increase in the $O^+ + N_2$ reaction rate [*St.-Maurice and Laneville*, 1998]. This would increase the altitude of transition from O^+-dominated to molecular ion-dominated ionospheres. *Kelly and Wickwar* [1981] found that the transition altitude deviates by, at most, ±30 km from Figure 6. As with the previously discussed T_e/T_i uncertainty, this level of uncertainty does not affect the conclusions of this paper.

4.2. Modeling O^+ Continuity

[23] We now describe a model that allows us to relate spectrometer measurements of the O^+ 732–733 nm brightness, all-sky measurements of arc morphology and residency time, and direct ISR measurements of $[O^+]$ in a quantitative way. The model exploits a critical distinction between chemical and photochemical equilibrium. Namely, the lifetime of O^+ against chemical recombination is much greater than the lifetime of the excited ^2P state of O^+ (produced by auroral ionization) against quantum mechanical deexcitation. The former is of order hours; the latter is about 5 s. We may thus assume photochemical equilibrium to connect the O^+ 732–733 nm intensity to O^+ production rate. We then use the optically derived O^+ production rate in a time-dependent continuity equation to estimate $[O^+]$.

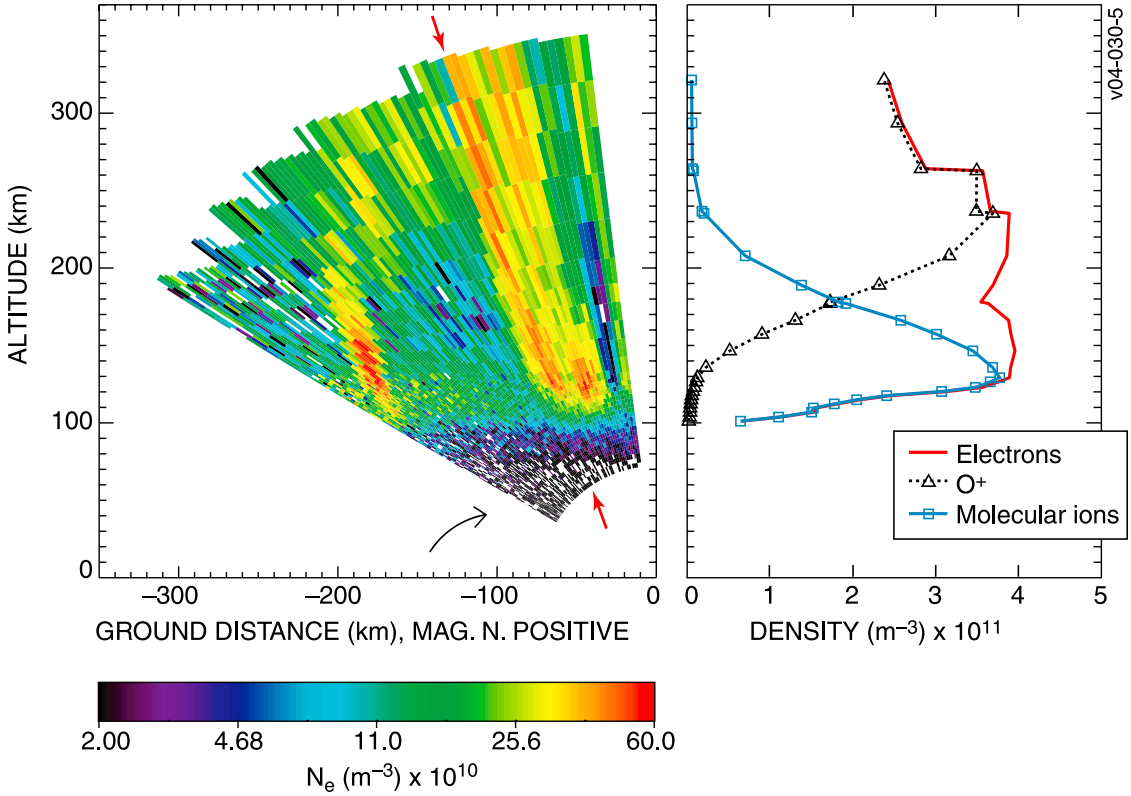

Figure 5. (a) Elevation scan for the 0101:56–0103:57 UT interval reprocessed at 1 s × 3 km (<150 km) and 12 km (>150 km) resolution, illustrating the undersampling of the spatial variability in Figure 3. (b) Total ion density (red curve), O^+ density (triangles), and molecular ion density (squares) extracted along the column bracketed by red arrows in Figure 5a.

[24] Impact of energetic electrons on ground-state atomic oxygen produces O^+ ions in one of three excited states:

$$\begin{aligned} O + e^* &\xrightarrow{0.4} O^+(^4S) + e^* + e^* - 13.61\text{eV} \\ O + e^* &\xrightarrow{0.4} O^+(^2D) + e^* + e^* - 16.92\text{eV} \\ O + e^* &\xrightarrow{0.2} O^+(^2P) + e^* + e^* - 18.61\text{eV}, \end{aligned} \quad (1)$$

with efficiencies (branching ratios) as indicated [*Rees*, 1989]. The transition from the metastable ^2P state to the ground ^4S state produces a quadruplet emission with wavelengths 731.89 nm, 732.0 nm, 732.97 nm, and 733.07 nm,

$$O^+(^2P) \xrightarrow{A_{2P}} O^+(^4S) + h\nu(732\text{ nm}), \quad (2)$$

that we refer to as O^+ 732–733 nm. The radiative lifetime of the ^2P state is ~5.27 s [*Zeippen*, 1987], so quenching reactions must be considered when relating $O^+(^2P)$ to the total O^+ density. The primary quenching agents are O, N_2, and, to a lesser extent, ambient electrons. Assuming photochemical equilibrium, the photon volume emission rate of O^+ 732–733 nm is related to the volume production O^+ ions by the expression

$$P_{732} = \frac{f_1 f_2 A_{2P}}{A_{2P} + K_O[O] + K_{N_2}[N_2] + K_e[e^-]} P_{O^+} \quad (3)$$

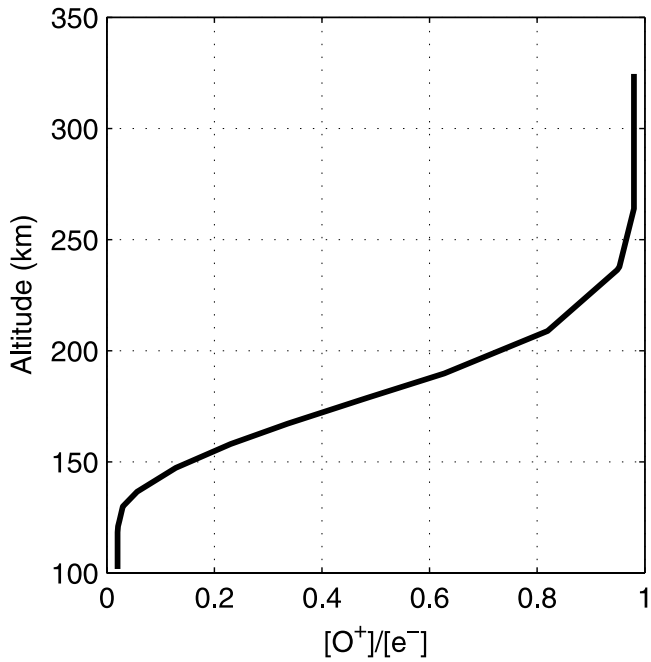

Figure 6. Ratio of O^+ density to total ion density as a function of altitude, used to compute Figure 5b.

Table 1. Dominant Chemical Loss Processes for Ionospheric O^+ in Units of cm^3/s

Reaction	Rate	Reference
$O^+ + N_2 \rightarrow NO^+ + N$	$K_1 = 2.78 \times 10^{-13}\exp\left[2.07\left(\frac{300}{T_i}\right) - 0.61\left(\frac{300}{T_i}\right)^2\right]$	*Chen et al.* [1978]
$NO^+ + e^- \rightarrow N + O$	$K_2 = 4.2 \times 10^{-7}\left(\frac{300}{T_e}\right)^{0.85}$	*Walls and Dunn* [1974] *Torr and Torr* [1977] *Alge et al.* [1983]
$O^+ + O_2 \rightarrow O_2^+ + O$	$K_3 = 3.23 \times 10^{-12}\exp\left[3.72\left(\frac{300}{T_i}\right) - 1.87\left(\frac{300}{T_i}\right)^2\right]$	*Chen et al.* [1978]
$O_2^+ + e^- \rightarrow O^* + O$	$K_4 = 1.95 \times 10^{-7}\left(\frac{300}{Te}\right)^{0.7}$	*Walls and Dunn* [1974] *Torr et al.* [1976]
$O^+ + e^- \rightarrow O^*$	$K_5 = 3.7 \times 10^{-12}(250/Te)^{0.7}$	*Dalgarno et al.* [1962]

[e.g. *Rusch et al.*, 1977; *Rees et al.*, 1982], with constants from *Rees et al.* [1982] as follows:

$$\begin{aligned} &\text{Fraction of radiating } O^+(^2P) \text{ in the multiplet} && f_1 = 0.781 \\ &\text{Branching ratio to the } {}^2P \text{ state} && f_2 = 0.2 \\ &\text{Transition probability} && A_{2_P} = 0.218 \\ &\text{Quenching by } N_2 && K_{N_2} = 4.8 \times 10^{-10}[\text{cm}^3/\text{s}] \\ &\text{Quenching by O} && K_O = 5.2 \times 10^{-11}[\text{cm}^3/\text{s}] \\ &\text{Quenching by electrons} && K_e = 1.89 \times 10^{-7} \cdot (T_e/300)^{1/2}[\text{cm}^3/\text{s}] \end{aligned} \tag{4}$$

computed by integration of (3),

$$\varepsilon_{732} = 10^{-6}\int_0^\infty P_{732}\,dl. \qquad \text{[Rayleighs]} \tag{5}$$

[25] It remains to relate P_{O+} to measurements of $[O^+]$. We do this through the continuity equation

$$\frac{d[O^+]}{dt} = P_{O^+} - L_{O^+} - \mathbf{V}\cdot\nabla[O^+]. \tag{6}$$

Let us consider the loss and transport terms on the right-hand side under the particular conditions of our event. Table 1 lists the primary reactions governing O^+ loss in the ionosphere. The dominant loss is through dissociative recombination in the upper two reaction chains. Direct recombination is a minor term since $[e^-] \ll [N_2], [O_2]$. The net loss rate is controlled by the slower reactions in the two dissociative recombination chains, namely,

$$L_O^+ \approx (K_1[N_2] + K_3[O_2])[O^+]. \tag{7}$$

[26] Figure 7 plots the time constant (or mean ion lifetime) for these two loss terms. The curves were computed using the MSIS-90 neutral atmosphere model for $[N_2]$ and $[O_2]$. We are concerned here with O^+ production over timescales of <3 min. Above 200 km, where the majority of O^+ is produced, the mean ion lifetime is $\gg$3 min. Thus to a good approximation, the loss term in the O^+ continuity equation can be neglected for the conditions of interest here.

[27] Consider now the transport term in (6). The observed columns extend from ~100 km, where transport is negligible, to >300 km, where transport is typically important. That the columns appear as contiguous structures across these altitude regimes, with a constant latitudinal width, provides strong evidence that the ionosphere production dominates horizontal transport over the entire altitude extent of the columns. Field-aligned transport may also be ruled out as a structuring mechanism owing to the long timescales for ambipolar diffusion compared to the ~3 min durations of interest here. In short, under the peculiar conditions of PBI auroras, namely, source duration of a few minutes and ion lifetime longer than a few minutes, the O^+ continuity equation reduces to

$$P_{O^+} = \frac{d[O^+]}{dt}. \tag{8}$$

[28] Combining (3), (5), and (8), we may write an expression relating the time rate of change of $[O^+]$ to ε_{732}:

$$\varepsilon_{732} = 10^{-6}\int_0^\infty \frac{f_1 f_2 A_{2_P}}{A_{2_P} + K_O[O] + K_{N_2}[N_2] + K_e[e^-]}\cdot\frac{d[O^+]}{dt}\,dl. \tag{9}$$

4.3. Self-Consistency of Radar and Optical Measurements

[29] We may use (9) to test the self-consistency of radar and optical observations. As a first approximation, we assume the ion production rate to be a constant over

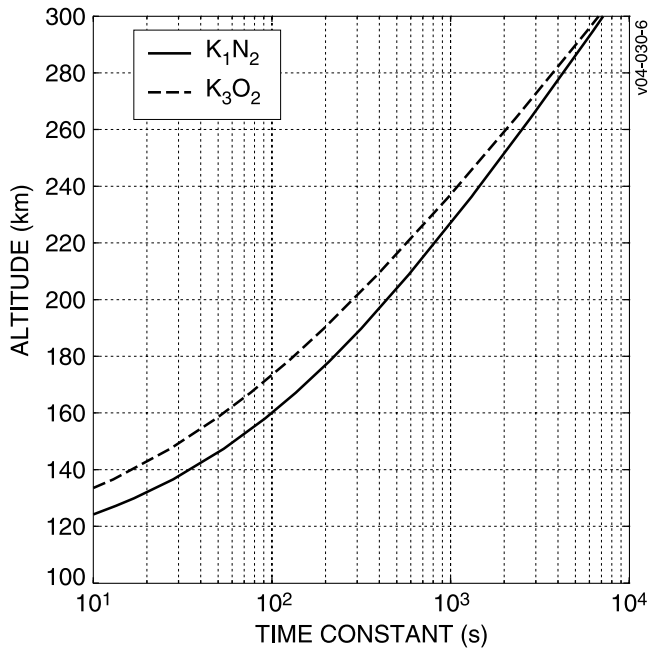

Figure 7. Time constant for the reactions $O^+ + N_2 \rightarrow O + NO^+$ (solid line) and $O^+ + O_2 \rightarrow O + O_2^+$ (dashed line).

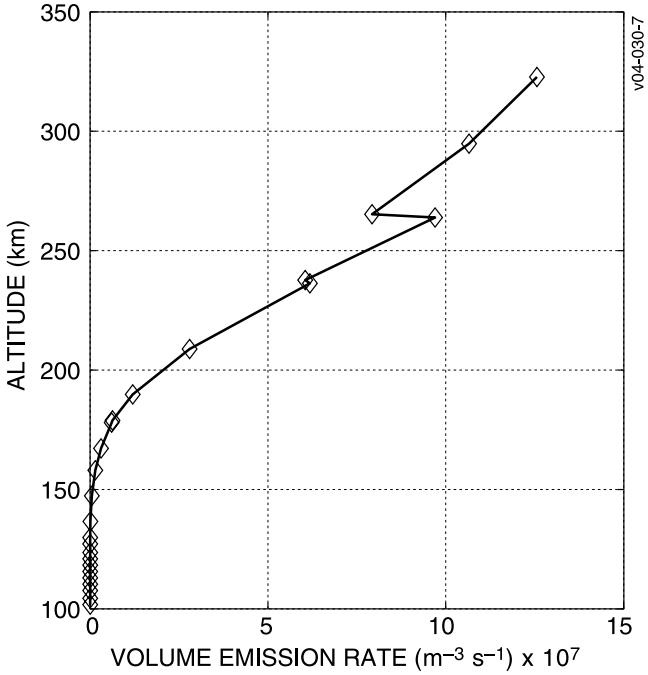

Figure 8. Volume emission rate profile for the O^+ 732–733 nm multiplet computed from equation (3). P_{O^+} was computed from equation (10) as described in the text.

duration Δt, such that the column-related density enhancement is given by $[O^+]_c = P_{O^+}\Delta t$, or

$$P_{O^+} \approx \frac{[O^+]_c}{\Delta t}. \quad (10)$$

Now we take Figure 5b (dashed curve) as $[O^+]_c$. From Figure 2, we conclude that this latitudinal region was illuminated for at least $\Delta t = 3$ min. Computing P_{O^+} from the above approximation and substituting into (3) gives the volume production curve for O^+ 732–733 nm plotted in Figure 8, where we have used the MSIS-90 model for background neutral densities [*Hedin*, 1991].

[30] The altitude of peak emission predicted from this model is clearly above the maximum altitude probed by the radar. The bottomside profile is, nonetheless, consistent with *Semeter* [2003], who analyzed O^+ 732–733 nm emission profiles using multispectral imagery for a series of arcs observed ~2 hours later on this same evening. In their analysis, the auroral flux tube was fixed in a physical coordinate system by ascribing a peak altitude of 120 km to the N_2 1PG emission layer. With this assumption, they found the peak altitude of the O^+ 732–733 nm multiplet layer to lie at ~380 km.

[31] Finally, using Figure 8 in equation (5), ε_{732} was computed numerically to be ~1.1 kR. Because Figure 8 does not capture the entire emission layer, we would expect this value to underestimate the observed maximum of 1.3 kR from Figure 4 by as much as a factor of 2. However, other uncertainties described earlier, including variations in source energy during this interval, exposure time of the NIR spectrograph, and uncertainties in the ISR coded-pulse analysis, probably contribute just as much uncertainty. This initial result is meant to show approximate agreement between observed columnar densities and measurements of production derived from independent optical sensors and to put forth an analytical framework in which future, higher-resolution measurements of oxygen aurora may be applied.

5. Consistency With Conjugate Particle Measurements

[32] Having confirmed the self-consistency of ground-based radar and optical diagnostics, we next investigated whether there exists a magnetospheric particle source capable of producing these features. We used measurements by the Fast Auroral Snapshot (FAST) satellite. Although precise conjugate measurements for the interval in Figure 5 were not available, we examined electron spectra for a PBI that occurred to the west of Sondrestrom ~35 min later. The location of FAST in relation to this intensification and the Sondrestrom facility is shown in Figure 9.

[33] Figure 10 shows burst-mode electron spectra measured at 1700 km within the 4730–4820 interval labeled in Figure 9. Note the presence of time-dispersive, counter-streaming populations (e.g., near labels 2 and 3). These are general indicators of electron energization by inertial Alfvén waves. Alfvén waves were detected sporadically throughout this interval (C. Chaston, personal communication, 2004). It is reasonable to expect that this combination of hard and soft spectra, with its high degree of spatial structuring, is representative of spectra responsible for the radar and optical measurements in Figures 1–4.

[34] To evaluate whether these electrons could account for the ionization columns of Figure 3, we appealed to a coupled model of electron penetration and ion continuity. Figure 11a plots the total differential number flux integrated over the source cone at times labeled 1, 2, and 3 in Figure 10. These samples represent different spectral morphologies observed: Spectrum 1 represents a typical ''bump on tail'' distribution commonly observed in energetic aurora. Spectrum 3 has a broad low-energy plateau typical of field-aligned bursts (FABs) [*Johnstone and Winningham*, 1982] produced by Alfvén wave acceleration. Spectrum 2 falls in between these regimes.

[35] Altitude profiles of ion production rate, q, were next computed for these spectra using a modified version of the *Rees* [1963] model of electron penetration, described in detail by *Semeter and Kamalabadi* [2005]. The results are shown in Figure 11b. To predict the resulting plasma density enhancement, we turn, once again, to the ionospheric continuity equation. We have previously shown that transport is expected to have a negligible effect in these ionization columns. We therefore included only production and loss terms:

$$\frac{d[e^-]}{dt} = p - r[e^-](K_1[N_2] + K_3[O_2]) - (1-r)K_2[e^-]. \quad (11)$$

Here, $[e^-]$ is the total plasma density, p is the total production rate of electron-ion pairs, and r is the ratio of $[O^+]$ to the total molecular ion density from *Kelly and Wickwar* [1981], also used in the analysis of Figure 5. In contrast with equation (10), which was only valid for the O^+

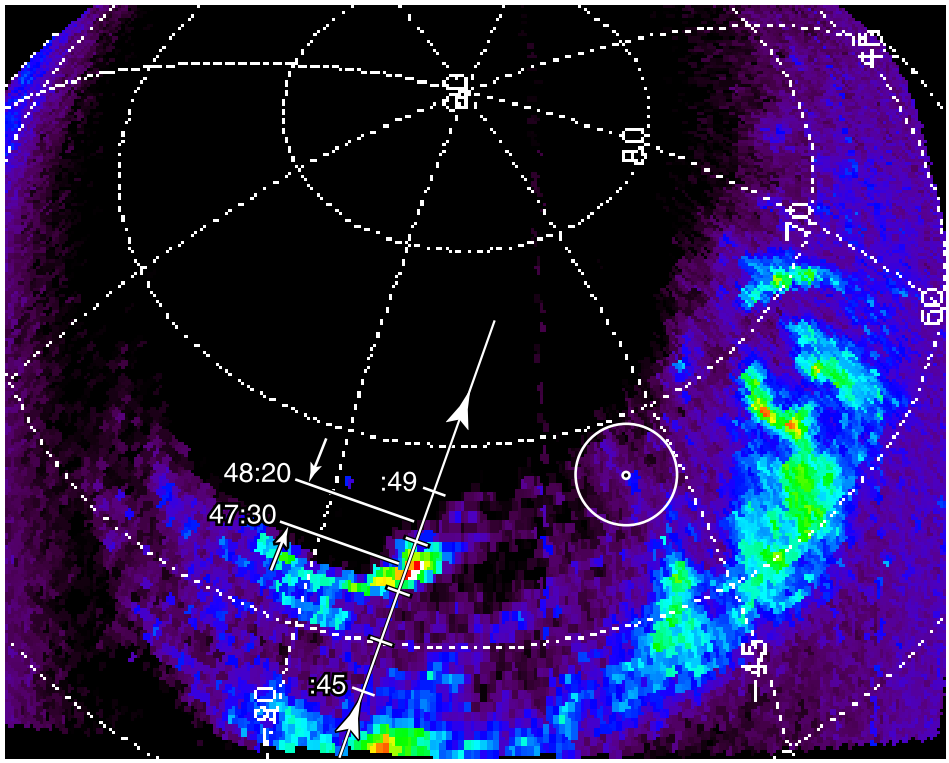

Figure 9. Auroral oval and FAST satellite track for the electron measurements presented in Figure 10, with geographic coordinates shown. Sondrestrom's location is indicated by the circle.

dominated F region, equation (11) is valid for the entire ionospheric extent of the flux tube. For this reason we must now included loss terms. The second term on the right-hand side accounts for F region recombination in a two-constituent neutral atmosphere, with recombination coefficients K_1 and K_3 as given in Table 1; the last term accounts for E region recombination assuming NO^+ is the dominant ion.

[36] Using Figure 11b in equation (11), plasma density profiles were computed numerically at various times. Results are shown in Figure 11c. The simulation was initialized with an arbitrary uniform density of 10^{10} m^{-3}, but similar results are obtained for 0 initial density. The critical point of Figure 11 is that plasma densities exceeding 10^{11} m^{-3} at 300 km can be readily achieved by the softer spectra (2 and 3) provided the flux tube is illuminated by these sources for at least 1 min. Under this requirement of source stability, the electron measurements of Figure 10 are consistent with the ionization structures of Figures 3 and 5.

[37] Note that for the hard spectrum (labeled 1), a density of 10^{11} m^{-3} is not reached at 300 km, even after 3 min. This ionization profile is similar to Figure 3 at 0057:51 and 0110:08 UT. Thus just as Figure 10 shows a mixture of hard and soft particle spectra within a PBI, so do the ground-based radar and optical measurements.

[38] Finally, we note that the forward model used to estimate p is most reliable for electrons of initial energy >500 eV (equivalent to penetration altitudes <180 km). As energy decreases, the ionization cross section increases such that more relative energy is deposited at higher altitudes. We thus expect the present model to underestimate the production rates above ~200 km, such that the ion densities above 200 km in Figure 11c would be achieved in a somewhat shorter period of time with a more accurate model.

6. Discussion

[39] We have examined particle spectra, optical forms, spectral emissions, and the ionization related to auroral intensifications along the active polar cap boundary. The study was motivated by the observations of narrow field-aligned columns of ionization embedded within regions of sustained rayed auroral forms associated with Alfvén wave-induced electron precipitation. Ionization columns were typically <5 km in cross section, extending in altitude from 100 to >300 km field-aligned altitude (Figures 3 and 5). The columns were coincident with intense emissions of O^+ 732–733 nm. In one case, the integrated O^+ 732–733 nm intensity exceeded 1.3 kR, a factor of ~4 brighter than any previously reported values.

[40] At altitudes greater than ~150 km, the ion lifetime is long compared with timescales associated with horizontal plasma transport through the radar volume. The interpretation of a plasma density enhancement in the auroral F region thus becomes ambiguous; horizontal transport and impact ionization can both produce latitudinally confined plasma structure. For this reason, we have coupled a model of O^+ ion continuity with a model of O^+ 732–733 nm photochemical equilibrium in an effort to test the self-consistency of simultaneous radar and optical measurements of these features. We found that the the the ISR observations of ion density were consistent with photometric estimates of O^+ production rate and all-sky camera measurements of arc residency time to within at least a factor of two. This result,

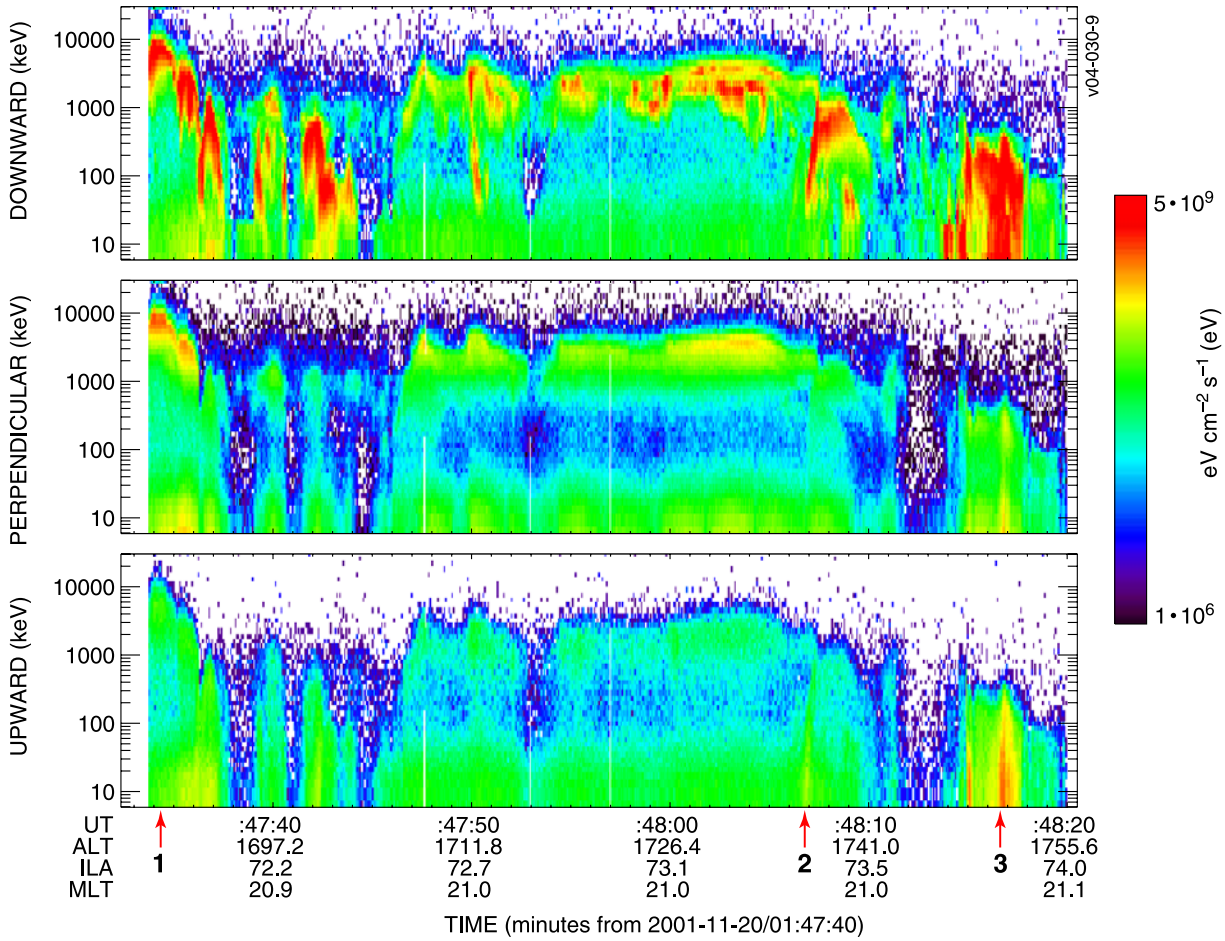

Figure 10. FAST burst-mode electron measurements for overflight of the poleward boundary intensification labeled in Figure 9.

along with the contiguous nature of the ionization columns, argues strongly that transport had a negligible impact on the *F* region density enhancements in Figure 3. The presence of such a localized ionizing flux at *F* region altitudes has also been confirmed by direct in situ measurement by sounding rocket [*Labelle et al.*, 1989].

[41] The width of the ionization columns was often observed to be uniform with altitude and the density distributed broadly in altitude. These observations place two important constraints on the causative electron source: (1) The illuminated flux tube must remain approximately stationary in the $E \times B$ reference frame for over a minute, and (2) the electron energies in the loss cone distribution must include both low energy (<100 eV) and high energy (>5 keV). The first constraint is required because an electron-ion pair produced above ~150 km is immediately locked into the background ionospheric convection pattern. If the auroral flux tube were not frozen into this motion, then the higher-altitude ionization would appear "smeared" in comparison with lower altitudes. This is not, in general, observed in Figures 3 and 5.

[42] The second constraint is required to account for the broad altitude distribution of the ionization. The particle spectrum on a given flux tube need not remain constant during the ionization buildup, but it must include a broad range of energies during its lifetime. Indeed, careful examination of Figure 2 shows that auroral intensity often varied significantly during a 2-min radar scan period, while the auroral morphology remained constant. The initial intensification from 0100:15 to 0101:03 UT, for instance, occurred with little distortion in the auroral forms. Auroral intensification without distortion provides additional evidence for a wave acceleration (i.e., nonelectrostatic) mechanism. If the acceleration were electrostatic, we should expect auroral brightening to be accompanied by an increase in the parallel potential drop experienced by the electrons. This, in turn, should increase the shear in the $E \times B$ flow field, leading to distortions in the optical forms [e.g., *Vogt et al.*, 1999]. Such effects are not observed in Figure 2.

[43] To determine whether electron precipitation in this region was consistent with our ground-based observations, we analyzed particle and field measurements by the FAST satellite over a PBI to the west of Sondrestrom. Alfvén waves were detected sporadically over this PBI, and electron spectra exhibited typical signatures of Alfvénic aurora [*Chaston et al.*, 2002]. Using a time-dependent model of electron penetration, we determined that these spectra could plausibly produce the observed plasma enhancements of $\sim 10^{11}$ m^{-3} at >300 km altitude, provided the source

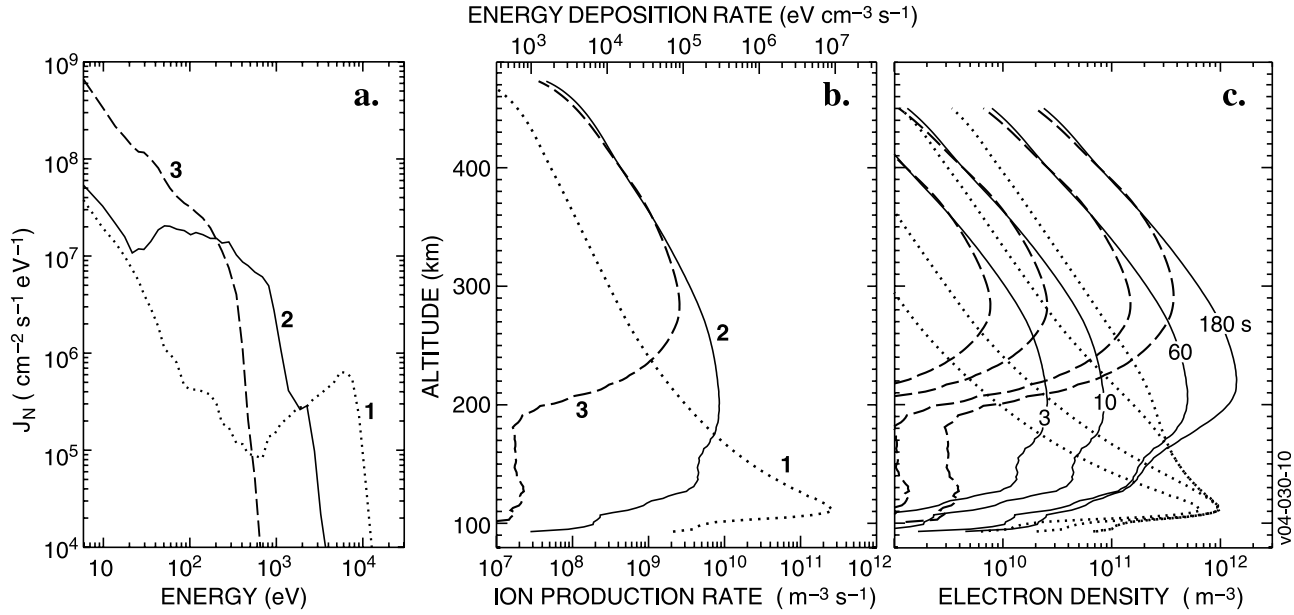

Figure 11. (a) Samples of downward differential number flux corresponding to the three labeled times in Figure 10. (b) Ionospheric production profiles computed for these spectra. (c) Ion density computed from equation (11) at several times, as indicated [after *Thayer and Semeter*, 2004].

remained fixed to a given flux tube within the ionospheric convection pattern for >1 min.

[44] The columns of Figure 3 are seen to be embedded within a nearly uniform *E* region layer centered at ~120 km. This layer requires a diffuse primary electron source of characteristic energy ~5 keV. The dispersive bursts of electrons in Figure 10 appear to be embedded in such a source (e.g., the 4746 to 4810 interval). Indeed, if one turns Figure 3 upside down, the appearance is qualitatively similar to Figure 10. It is thus reasonable to speculate whether the field-aligned "bursts" in Figure 10 are responsible for the ionization columns. The best way to resolve the spatial-temporal ambiguity implied by this question is through the use of spectral imagery. High-speed, high-resolution imaging of a prompt near-infrared emissions, such as O 844.6 nm, would be particularly useful.

[45] The event studied here is consistent with *Lyons et al.* [2000] designation of a PBI. However, the principal defining characteristic of these auroras, namely, a region of bright Alfvénic aurora poleward of the main auroral oval, also describes the transient behavior of the auroral oval near substorm onset [*Mende et al.*, 2003]. Thus the dynamic magnetosphere-ionosphere equilibrium under which PBIs occur could be described as a continuous state of substorm onset. A major difference between PBIs and substorm aurora has to do with the residency time of the wave accelerated electron fluxes. The tall columns of ionization observed in Figure 3 would not be an expected consequence of the more ephemeral substorm onset arc, even if the requisite particle spectra are present.

7. Summary and Conclusions

[46] We have investigated the detailed ionospheric response to a Poleward Boundary Intensification (PBI). Observations of narrow field-aligned columns of enhanced plasma (Figures 3 and 5) were found to be consistent with photometric measurements of ion production (Figure 4). In situ measurements of field-aligned electron bursts measured in near-conjugation to this event (Figure 10) could plausibly produce these features, provided they remain stationary in the $E \times B$ reference frame for at least 1 min. These spectra were observed in a region of intense Alfvén wave activity.

[47] The results presented herein have two important consequences for magnetosphere-ionosphere coupling. The first concerns horizontal gradients. The structures imaged in Figure 3 correspond to large gradients in ionospheric conductivity. In fact, we argue that although the largest aurorally enhanced conductance may be produced within substorm breakup, the largest gradients in conductance occur within these poleward boundary intensifications. If field-aligned currents are closed in this region, we would expect small-scale polarization electric fields to be distributed throughout this region and hence significant spatial variability in the Joule dissipation rate [e.g., *Codrescu et al.*, 1995].

[48] The second consequence concerns the optical morphology of PBI arcs as compared with substorm breakup aurora. PBI arcs are more ray-like than arc-like (e.g., Figure 2), leading to the possibility of more cylindrical ionization patterns. This means that horizontal gradients in conductivity can be large in any direction, including the $E \times B$ direction. Gradients in the $E \times B$ direction will be unstable to the gradient-drift instability. The columns of Figure 3 may therefore cascade to smaller-scale structures as a consequence of this unstable ionization geometry [*Dyrud et al.*, 2004].

[49] **Acknowledgments.** The authors are grateful to E. M. Blixt, C. Chaston, and J. P. Thayer, for helpful discussions, and to M. McCready for data preparation. This work was supported by the National Science Foundation under grants ATM-0302672 and ATM-9317167,

OPP-9910950, OPP-0337618, and OPP-0352742, and by NASA under grants NAGS-12979, and NAGS-13592.

[50] Arthur Richmond thanks James LaBelle and Dirk Lummerzheim for their assistance in evaluating this paper.

References

Arnoldy, R., K. Lynch, and J. Austin (1999), Energy and pitch angle-dispersed aurora electrons suggesting a time-variable inverted-V potential structure, *J. Geophys. Res.*, *104*, 22,613.

Chaston, C. C., J. W. Bonnell, L. M. Peticolas, C. W. Carlson, J. P. McFadden, and R. E. Ergun (2002), Driven Alfven waves and electron acceleration: A FAST case study, *Geophys. Res. Lett.*, *29*(11), 1535, doi:10.1029/2001GL013842.

Codrescu, M. V., T. J. Fuller-Rowell, and J. C. Foster (1995), On the importance of E-field variability for Joule heating in the high-latitude thermosphere, *Geophys. Res. Lett.*, *22*, 2393–2396.

Crowley, G., A. J. Ridley, D. Deist, S. Wing, D. J. Knipp, B. A. Emery, J. Foster, M. Hairston, and B. W. Reinisch (2000), Transformation of high-latitude ionospheric *F*-region patches into blobs during the March 21, 1990, storm, *J. Geophys. Res.*, *105*, 5215–5230.

Dyrud, L., J. Semeter, and M. Oppenheim (2004), Plasma instabilities in auroral ionospheric density gradients from 120–200 km altitude, *Eos Trans. AGU*, *85*(17), Jt. Assem. Suppl., Abstract SM51A-0338.

Elphinstone, R. D., et al. (1995), The double oval UV auroral distribution, 1. implications for the mapping of auroral arcs, *J. Geophys. Res.*, *100*, 12,075–12,092.

Evans, J. (1969), Theory and practice of ionospheric study by Thomson scatter radar, *Proc. IEEE*, *57*, 496–530.

Hedin, A. (1991), Extension of the MSIS thermosphere model into the middle and lower atmosphere, *J. Geophys. Res.*, *96*, 1159–1172.

Henderson, M. G., G. D. Reeves, and J. S. Murphree (1998), Are north-south aligned auroral structures an ionospheric manifestation of bursty bulk flows?, *Geophys. Res. Lett.*, *25*, 3737–3740.

Johnstone, A. D., and J. D. Winningham (1982), Satellite observations of suprathermal electron bursts, *J. Geophys. Res.*, *87*, 2321.

Kelly, J. D., and V. B. Wickwar (1981), Radar measurements of high-latitude ion composition between 140 and 300 km altitude, *J. Geophys. Res.*, *86*, 7617–7626.

Labelle, J., R. J. Sica, C. Kletzing, G. D. Earle, and M. C. Kelley (1989), Ionization from soft electron precipitation in the auroral F region, *J. Geophys. Res.*, *94*, 3791–3798.

Lyons, L. R., E. Zesta, J. C. Samson, and G. D. Reeves (2000), Auroral disturbances during the January 10, 1997 magnetic storm, *Geophys. Res. Lett.*, *27*, 3237–3240.

Lyons, L. R., E. Zesta, Y. Xu, E. R. Sánchez, J. C. Samson, G. D. Reeves, J. M. Ruohoniemi, and J. B. Sigwarth (2002), Auroral poleward boundary intensifications and tail bursty flows: A manifestation of a large-scale ULF oscillation?, *J. Geophys. Res.*, *107*(A11), 1352, doi:10.1029/2001JA000242.

Mende, S. B., C. W. Carlson, H. U. Frey, L. M. Peticolas, and N. Østgaard (2003), FAST and IMAGE-FUV observations of a substorm onset, *J. Geophys. Res.*, *108*(A9), 1344, doi:10.1029/2002JA009787.

Rees, M. (1963), Auroral ionization and excitation by incident energetic electrons, *Planet. Space Sci.*, *11*, 1209–1218.

Rees, M. (1989), *Physics and Chemistry of the Upper Atmosphere*, Cambridge Univ. Press, New York.

Rees, M. H., V. J. Abreu, and P. B. Hays (1982), The production efficiency of O^+ (^2P) ions by auroral electron impact ionization, *J. Geophys. Res.*, *87*, 3612–3616.

Robinson, R., R. Tsunoda, J. Vickrey, and L. Guerin (1985), Sources of *F*-region ionization enhancements in the nighttime auroral zone, *J. Geophys. Res.*, *90*, 7533–7546.

Rusch, D. W., D. G. Torr, P. B. Hays, and J. C. G. Walker (1977), The OII (7319–7330 Å) dayglow, *J. Geophys. Res.*, *82*, 719–722.

Semeter, J. (2003), Critical comparison of OII (732–733 nm), OI (630 nm), and N_2 (1PG) emissions in auroral rays, *Geophys. Res. Lett.*, *30*(5), 1225, doi:10.1029/2002GL015828.

Semeter, J., and F. Kamalabadi (2005), Determination of primary electron spectra from incoherent scatter radar measurements of the auroral *E* region, *Radio Sci.*, *40*, RS2006, doi:10.1029/2004RS003042.

Semeter, J., C. J. Heinselman, J. P. Thayer, R. A. Doe, and H. U. Frey (2003), Ion upflow enhanced by drifting F-region plasma structure along the nightside polar cap boundary, *Geophys. Res. Lett.*, *30*(22), 2139, doi:10.1029/2003GL017747.

Sivjee, G. G., and D. Shen (1997), Auroral optical emissions during the solar magnetic cloud event of October 1995, *J. Geophys. Res.*, *102*, 7431–7438.

St.-Maurice, J.-P., and P. J. Laneville (1998), Reaction rate of O^+ with O_2, N_2, and *NO* under highly disturbed auroral conditions, *J. Geophys. Res.*, *103*, 17,519–17,522.

Thayer, J., and J. Semeter (2004), The convergence of magnetospheric energy flux in the polar atmosphere, *J. Atmos. Sol. Terr. Phys.*, *66*, 805–817.

Vogt, J., H. Frey, G. Haerendel, H. Hoefner, and J. Semeter (1999), Shear velocity profiles associated with auroral curls, *J. Geophys. Res.*, *104*, 17,277–17,288.

Yamamoto, T., et al. (1993), Meridional structures of electric potentials relevant to premidnight discrete auroras: A case study from Akebono measurements, *J. Geophys. Res.*, *98*, 11,135–11,152.

Zeippen, C. (1987), Improved radiative transition probabilities for O-II forbidden lines, *Astron. Astrophys.*, *173*, 410–414.

Zesta, E., E. Donovan, L. Lyons, G. Enno, J. S. Murphree, and L. Cogger (2002), Two-dimensional structure of auroral poleward boundary intensifications, *J. Geophys. Res.*, *107*(A11), 1350, doi:10.1029/2001JA000260.

J. W. Bonnell and H. U. Frey, Space Sciences Laboratory, University of California, Berkeley, 7 Gauss Way, Berkeley, CA 94720-7450, USA.

C. J. Heinselman, SRI International, 333 Ravenswood Avenue, Menlo Park, CA 94061, USA.

J. Semeter, Department of Electrical and Computer Engineering and Center for Space Physics, Boston University, 8 Saint Mary's St., Boston, MA 02215, USA. (jls@bu.edu)

G. G. Sivjee, Embry-Riddle Aeronautical University, 600 South Clyde Morris Boulevard, Daytona Beach, FL 32114, USA.